ELSEVIER

Journal of Crystal Growth 193 (1998) 552–562

JOURNAL OF CRYSTAL GROWTH

Theoretical analysis of the micro-pulling-down process for Ge_xSi_{1-x} fiber crystal growth

C.W. Lan[a,]*, S. Uda[b], T. Fukuda[c]

[a] Department of Chemical Engineering, National Taiwan University, Taipei 10617, Taiwan, ROC
[b] Central Research Institute, Mitsubish Materials Co. Ltd., 1-297 Kitabukuro-Cho, Omiya, Saitama 330, Japan
[c] Institute of Materials Research, Tohoku University, 2-1-1 Katahira, Aoba-ku, Sendai 980-77, Japan

Received 29 December 1997; accepted 2 June 1998

Abstract

Theoretical analysis of the micro-pulling-down process for the growth of Ge_xSi_{1-x} single crystal fibers is conducted using a finite-volume/Newton's method. Steady-state heat and nondilute solute transfer, melt flow, the melt/crystal interface, and the free surface as well as the grown fiber diameter are solved simultaneously. The effects of process parameters including the melt height, the die temperature, and the growth rate on the grown fiber diameter and solute distribution are investigated. Good agreement is found for the calculated meniscus shape and the grown fiber diameter with the observed ones. In the melt zone, due to the small physical dimension and the damping effect by Ge, buoyancy convection is negligible. However, Marangoni convection is dominant there and the solute segregation is thus affected. As the melt zone becomes shorter with the decreasing die temperature, a secondary flow is induced by the Marangoni convection leading to an inversion on radial segregation and a large depletion of Ge in the fiber core, which are consistent with the measurements. © 1998 Published by Elsevier Science B.V. All rights reserved.

PACS: 44.25.+f; 47.27.Te; 81.10.Fg; 02.60.Cb; 02.70.Fj

Keywords: Micro-pulling-down; Fiber growth; Computer simulation; Convection; Segregation

1. Introduction

The unique properties of near one-dimensional single crystal fibers have attracted some attention on the applications of optical and electronic devices [1–3]. The device-size as-grown fibers also reduce processing cost (for size reduction) significantly for device fabrication. There are several methods for growing fiber crystals [4], such as the edge-defined film-fed growth (EDFG), floating zone (pedestal growth) methods, etc. Recently, the micro-pulling-down (μ-PD) process, a variant of the inverse EDFG, developed by Fukuda's laboratory in Japan [5–9] has been shown promising in producing single crystal fibers with good diameter

---

*Corresponding author. Fax: + 886 2 2363 3917; e-mail: lan@ruby.che.ntu.edu.tw.

PII: S0022-0248(98)00527-2

control and concentration uniformity. Several oxide [5–7] and semiconductor fibers [8,9] have been grown. The grown diameter ranges from 10 to 1500 μm for oxides and about 300 to 900 μm for semiconductors. Because of the high thermal gradients near the growth interface, it is also possible to use a very high growth rate (several centimeters per hour) without causing constitutional supercooling that leads to interface breakdown. In this process, some simple theoretical analyses for the operation limit [10] and solute distribution [11,12] have been performed. However, no detailed modeling has been conducted. Especially, the melt convection was ignored in the previous reports. In fact, even for EDGF, detailed convective heat and mass transfer simulation coupled with the capillary shaping and the solidification has not been reported as well. Since the system is small, the measurements of concentration and temperature are difficult. Furthermore, although buoyancy convection may be negligible due to the small physical dimension, thermocapillary convection (Marangoni flow) may be still important because of the high thermal gradients near the growth interface. Therefore, a detailed numerical simulation will allow crystal growers to better "visualize" the process, and thus provide a foundation for process improvement and tuning.

In this study, a detailed numerical simulation is conducted in a self-consistent manner to analyze the μ-PD process for Ge_xSi_{1-x} fibers; $x = 0.05$. The melt flow, heat and mass transfer, the growth front and meniscus, and the grown fiber diameter for various process parameters are illustrated. The role of convection on solute transport will be emphasized. Some comparison with simple models for capillary shaping and solute diffusion as well as experimental observations is also performed. The model formulation and the solution scheme are described in the next section. Section 3 is devoted to the results and discussion, followed by conclusions in Section 4.

2. Model and solution scheme

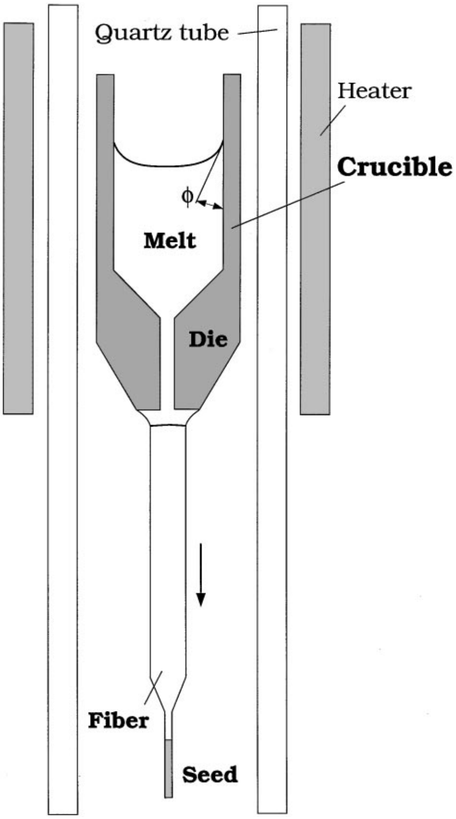

Fig. 1. Schematic diagram of the micro-pulling-down fiber growth process.

The system to be modeled is sketched in Fig. 1. Since the melt height and the grown fiber length are much larger than the zone dimension (the area between the die and the growth front), to relieve computational load, while balancing model accuracy, the computational domain is chosen for the part near the melt zone only, as shown in Fig. 2a. Since the melt height is much larger than the length of the capillary tube, a good approximation is to ignore the melt reservoir (the crucible), but including the melt height into account for meniscus calculation. Furthermore, it is believed that the melt flow in the reservoir does not affect much the flow inside the channel as well as the melt zone. In addition, the melt velocity at the top entrance (at $z = -L_h$) is assumed uniform. If a pseudo-steady state is achieved for the fiber pulling rate U_c, the melt velocity U_m at the upper boundary from the melt reservoir can be set to be $\rho_c U_c (R_c/R_h)^2/\rho_m$; ρ_c and ρ_m are the crystal and melt densities, respectively.

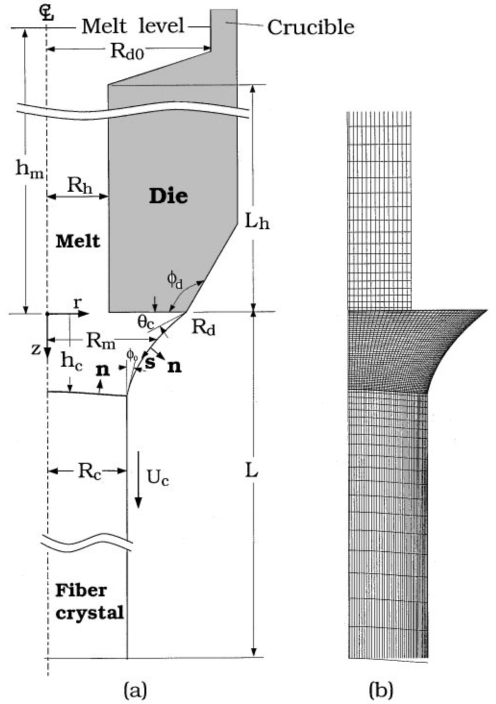

Fig. 2. (a) Schematic diagram of the computational domain; (b) a portion of a sample mesh for calculation.

Usually, the charge of the feed material is about 2 g, and the amount of the grown crystal is only 1 or 2% of the charge. Therefore, the change of the top melt level is very small. In fact, in practice, it is important to have enough melt for the fiber growth, and that can ensure the steadiness of the process, especially, for capillary shaping; the effect of the melt height will be illustrated shortly. The top meniscus of the melt in the crucible is considered through the effective melt head h_{eff}, which will be explained shortly as well. The die temperature is assumed to be a linear distribution along the axial distance from $z = 0$. Furthermore, a perfect attachment of the melt along the die edge is assumed.

Axisymmetry is further assumed. Hence, the melt velocity, temperature, solute concentration, and the free surface ($R_{\mathrm{m}}(z)$), as well as the growth front ($h_{\mathrm{c}}(r)$), are represented in cylindrical coordinate system (r, z). It is also assumed that the solute is uniformly distributed in the melt reservoir and its concentration is C_0. Dimensionless variables are defined by scaling length by R_{d}, velocity by $\alpha_{\mathrm{m}}/R_{\mathrm{d}}$, temperature by the melting point T_{m} of silicon $(x = 0)$, and concentration by C_0, where α_{m} is the thermal diffusivity of the melt. For the convenience of representation, all the variables defined afterwards are dimensionless unless otherwise stated. The governing equations in the conservative-law form (or the so-called divergence form) for melt flow and heat and solute transfer can be described in terms of stream function ψ, vorticity ω, temperature T, and concentration C as follows:

Equation of motion

$$\frac{\partial}{\partial r}\left(\frac{\omega}{r}\frac{\partial \psi}{\partial z}\right) - \frac{\partial}{\partial z}\left(\frac{\omega}{r}\frac{\partial \psi}{\partial r}\right) + \mathrm{Pr}\left[\frac{\partial}{\partial r}\left(\frac{1}{r}\frac{\partial}{\partial r}(r\omega)\right) + \frac{\partial}{\partial z}\left(\frac{1}{r}\frac{\partial}{\partial z}(r\omega)\right)\right] - \mathrm{Pr}\mathrm{Ra}_{\mathrm{T}}\frac{\partial T}{\partial r} + \mathrm{Pr}\mathrm{Ra}_{\mathrm{S}}\frac{\partial C}{\partial r} = 0. \tag{1}$$

Stream equation

$$\frac{\partial}{\partial z}\left(\frac{1}{r}\frac{\partial \psi}{\partial z}\right) + \frac{\partial}{\partial r}\left(\frac{1}{r}\frac{\partial \psi}{\partial r}\right) + \omega = 0. \tag{2}$$

Energy equation

$$-\frac{\partial}{\partial r}(ruT) - \frac{\partial}{\partial z}(rvT) + \frac{\partial}{\partial z}\left(r\alpha_i(T)\frac{\partial T}{\partial z}\right) + \frac{\partial}{\partial r}\left(r\alpha_i(T)\frac{\partial T}{\partial r}\right) = 0, \quad i = (\mathrm{m}, \mathrm{c}). \tag{3}$$

Solute equation

$$-\frac{\partial}{\partial r}(ruC) - \frac{\partial}{\partial z}(rvC) + \frac{\mathrm{Pr}}{\mathrm{Sc}}\left[\frac{\partial}{\partial z}\left(r\frac{\partial C}{\partial z}\right) + \frac{\partial}{\partial r}\left(r\frac{\partial C}{\partial r}\right)\right] = 0. \tag{4}$$

The solute diffusion in the solid phase is neglected. In the above equations, Pr is the Prandtl number ($\mathrm{Pr} \equiv \alpha_{\mathrm{m}}/\nu_{\mathrm{m}}$, where ν_{m} is the kinematic melt viscosity), Sc the Schmidt number ($\mathrm{Sc} \equiv \nu_{\mathrm{m}}/D$), and D the diffusivity of germanium in the melt. Also, α_i is the thermal diffusivity of phase i; $i = \mathrm{c}$ for crystal and m for melt. Two important dimensionless variables, Ra_{T} and Ra_{S}, in the source term of the equation of motion are defined as follows:

$$\mathrm{Ra_T} \equiv \frac{g\beta_\mathrm{T} T_\mathrm{m} R_\mathrm{d}^3}{\alpha_\mathrm{m}\nu_\mathrm{m}}; \quad \mathrm{Ra_S} \equiv \frac{g\beta_\mathrm{S} C_0 R_\mathrm{d}^3}{\alpha_\mathrm{m}\nu_\mathrm{m}},$$

where g is the gravitational acceleration and β_T and β_S are the thermal and solutal expansion coefficients, respectively. The stream function ψ and vorticity ω in the above equations are defined in terms of the radial (u) and axial (v) velocities as:

$$u = -\frac{1}{r}\frac{\partial\psi}{\partial z}, \quad v = \frac{1}{r}\frac{\partial\psi}{\partial r}, \tag{5}$$

$$\omega = \frac{\partial u}{\partial z} - \frac{\partial v}{\partial r}. \tag{6}$$

To solve the above governing equations, boundary conditions are also required. Most of the boundary conditions for melt flow and heat and mass transfer can be found elsewhere [13]. Only some important boundary conditions are described here. The solute boundary conditions at the top entrance ($z = -L_\mathrm{h}$) is set by the solute flux balance:

$$\boldsymbol{e}_z \cdot \nabla C = \left(\frac{\mathrm{Sc}}{\mathrm{Pr}}\right)\mathrm{Pe_m}(C-1). \tag{7}$$

At the melt/crystal interface,

$$\boldsymbol{n} \cdot \nabla C = \left[\left(\frac{\rho_\mathrm{c}}{\rho_\mathrm{m}}\right) - K\right]\left(\frac{\mathrm{Sc}}{\mathrm{Pr}}\right)\mathrm{Pe_c} C(\boldsymbol{n}\cdot\boldsymbol{e}_z), \tag{8}$$

where $\boldsymbol{n}$ is the unit normal vector at the growth front pointing to the melt, $\mathrm{Pe_m} \equiv U_\mathrm{m} R_\mathrm{d}/\alpha_\mathrm{m}$ and $\mathrm{Pe_c} \equiv U_\mathrm{c} R_\mathrm{d}/\alpha_\mathrm{m}$ are the Peclect numbers of the melt and crystal, respectively, and K is the segregation coefficient according to the phase diagram. The density ratio ($\rho_\mathrm{c}/\rho_\mathrm{m}$) is considered, but its effect is small. Again, the solid state diffusion in the crystal is neglected here.

For the meniscus shape, the normal stress balance is used:

$$\boldsymbol{nn}: t - \mathrm{Bo}(z + h_\mathrm{eff}) = 2H, \tag{9}$$

where $\boldsymbol{n}$ is the unit normal vector at the free surface pointing outward and t the shear stress tensor. $\mathrm{Bo} \equiv \rho_\mathrm{m} g R_\mathrm{d}^2/\gamma$ is the Bond number measuring the relative effects of gravity and surface tension, and h_eff the dimensionless effective melt height from $z = 0$; γ is the surface tension coefficient. If we know the static contact angle ϕ (see Fig. 1) and the dimensionless average melt height h_m, a simple approximation may be used to calculate h_eff:

$$h_\mathrm{eff} = h_\mathrm{m} - 2\mathrm{Bo}^{-1}\cos(\phi) R_\mathrm{d}/R_\mathrm{d0}, \tag{10}$$

where R_d0 is the inner radius of the crucible. Apparently, if the crucible radius is small and the crucible can be wetted by the melt ($\phi \leqslant 90°$), h_eff can be smaller than the melt height h_m. In reality, it is not easy to accurately determine ϕ because the graphite reacts with Si and thus the wetting angle is changed. Therefore, we will use h_eff in the calculation and its effects can then be illustrated, which reflect the effects of the meniscus as well as the melt height.

In order to grow the fiber with a constant diameter, the growth angle constraint [14] needs to be specified:

$$\mathrm{d}R_\mathrm{m}/\mathrm{d}z = -\tan(\phi_0), \tag{11}$$

where ϕ_0 is the growth angle. For example, $\phi_0 = 11°$ for Si in $\langle 1\,1\,1\rangle$ growth direction. However, the steadily grown fiber radius R_c is unknown a priori and needs to be calculated.

The tangential stress balance for the free surface is further required:

$$\boldsymbol{ns}: t = \mathrm{Ma}(\boldsymbol{s}\cdot\nabla T), \tag{12}$$

where $\boldsymbol{s}$ is the unit tangent vector at the free surface and the Marangoni number $\mathrm{Ma} \equiv (\partial\gamma/\partial T) R_\mathrm{d} T_\mathrm{m}/(\mu_\mathrm{m}\alpha_\mathrm{m})$; $\partial\gamma/\partial T$ is the surface-tension-temperature coefficient and μ_m the melt viscosity.

The die temperature is assumed as a linear function of the axial distance, i.e., $T_\mathrm{d}(z) = T_\mathrm{d}|_0 - (T_\mathrm{d}|_{L_\mathrm{h}} - T_\mathrm{d}|_0)z/L_\mathrm{h}$. At the surface of material, heat transfer from the system to the ambient is by both radiation and convection according to the energy balance along the material surface:

$$-\boldsymbol{n}\cdot\kappa_i\nabla T = \mathrm{Bi}(T - T_\mathrm{a}) + \mathrm{Rad}_i(T^4 - T_\mathrm{a}^4),$$
$$i = (\mathrm{m}, \mathrm{c}), \tag{13}$$

where $\boldsymbol{n}$ is the unit normal vector on the melt or crystal surface pointing outwards, κ_i the ratio of thermal conductivity of phase i to the melt, $\mathrm{Bi} \equiv hR_\mathrm{d}/k_\mathrm{m}$ the Biot number, and $\mathrm{Rad}_i \equiv \sigma\varepsilon_i T_\mathrm{m}^3 R_\mathrm{d}/k_\mathrm{m}$ the radiation number; σ is the Stefan–Boltzmann constant, while ε_i is the surface emmisivity of the melt or crystal. T_a is the effective ambient temperature, and it is set to be a constant in this study.

At the end of the fiber in the domain ($z = L$), the zero flux boundary condition is used. The length L is made large enough so that the calculated molten zone length is insensitive to its value. L being 100 times of R_d is found satisfactory. Furthermore, using the fixed-temperature boundary condition, i.e, $T = T_\mathrm{a}$ at $z = L$, does not change the results much.

The governing equations with their associated boundary conditions are discretized by a finite volume method (FVM) [15]. A portion of a converged sample mesh for calculation is shown in Fig. 2b, where the meniscus shape, the growth interface, and the grown fiber radius are unknown a priori, and need to be solved with filed variables simultaneously. After the FVM approximation, the resulting nonlinear equations are then solved by Newton's method globally. Usually, five to seven iterations are enough for the solution to converge to an infinity norm of 10^{-6}. Details of the numerical scheme can be found elsewhere [15,16].

3. Results and discussion

The physical properties of $\mathrm{Ge}_x\mathrm{Si}_{1-x}$ and some input parameters used in calculations are listed in Table 1. Since x is small (0.05), most of the physical properties of Si are adopted. The liquidus slope and the segregation coefficient are obtained from the phase diagram. In the present study, we are interested only in cases with $x = 0.05$, which was used in the previous experiments [12]. Also, the diffusivity values of Ge in Si from different reports [9,12,17] are quite different. However, according to a recent report [12], $D = 5.6 \times 10^{-5}\ \mathrm{cm^2/s}$ seems to be more reasonable, and thus this value is used here. Before the results were presented, we also performed mesh refinement to ensure that the solution is not affected much by the mesh. Due to the large Sc value, the solute boundary layer is much thinner than the velocity one. Therefore, fine grid spacing near the solid boundaries is necessary. A part of the sample mesh used in our calculations is shown in Fig. 2b. The number of unknowns resulted from this mesh is 16 459, and one Newton's iteration takes about 1 min in an HP9000/C180 workstation.

Table 1

Physical properties of $\mathrm{Ge}_{0.05}\mathrm{Si}_{0.95}$ and some input parameters

Physical properties

$T_\mathrm{m} = (1683.4–220x)\ \mathrm{K}$
$\Delta H = 1803\ \mathrm{J\ g^{-1}}$
$k_\mathrm{c} = 0.22\ T_\mathrm{m}/T\ \mathrm{W\ cm^{-1}\ K^{-1}}$
$k_\mathrm{m} = 0.64\ \mathrm{W\ cm^{-1}\ K^{-1}}$
$Cp_\mathrm{c} = 1.038\ \mathrm{J\ g^{-1}\ K^{-1}}$
$Cp_\mathrm{m} = 1.059\ \mathrm{J\ g^{-1}\ K^{-1}}$
$\partial\gamma/\partial T = -0.08\ \mathrm{dyn\ cm^{-1}\ K^{-1}}$
$\gamma = 720 + (T - T_\mathrm{m})\partial\gamma/\partial T\ \mathrm{dyn\ cm^{-1}}$
$\mu_\mathrm{m} = 0.007\ \mathrm{g\ cm^{-1}\ s^{-1}}$
$\beta_\mathrm{s} = 0.013/(\mathrm{at\ \%Ge})$
$\beta_\mathrm{T} = 1 \times 10^{-4}\ \mathrm{K^{-1}}$
$\varepsilon_\mathrm{c} = 0.7$
$\varepsilon_\mathrm{m} = 0.3$
$\rho_\mathrm{c} = 2.33\ \mathrm{g\ cm^{-3}}$
$\rho_\mathrm{m} = 2.55\ \mathrm{g\ cm^{-3}}$
$K = 0.4$
$\phi_0 = 11^\circ$

Input parameters

$R_\mathrm{h} = 0.0275\ \mathrm{cm}$
$R_\mathrm{d} = 0.057\ \mathrm{cm}$
$L_\mathrm{h} = 0.33\ \mathrm{cm}$
$L = 3\ \mathrm{cm}$
$T_\mathrm{d}|_0 = 1673.4–1676.4\ \mathrm{K}$
$T_\mathrm{d}|_{-L_\mathrm{h}} = 1683.4\ \mathrm{K}$
$T_\mathrm{a} = 635.4\ \mathrm{K}$
$U_\mathrm{c} = 1–6\ \mathrm{cm/h}$
$h = 4.4 \times 10^{-3}\ \mathrm{W\ cm^{-2}\ K^{-1}}$
$C_0 = 5\ \mathrm{at\%}$

3.1. Meniscus shape and grown fiber size

The meniscus shape as well as the grown fiber diameter is mainly affected by the capillary statics and the melt height. The effect of melt convection is believed to be trivial, which will be shown shortly. Fig. 3a shows the calculated meniscus shapes for different h_eff's; the grown fiber diameter is fixed and the growth angle $\phi_0 = 11^\circ$. An observed meniscus

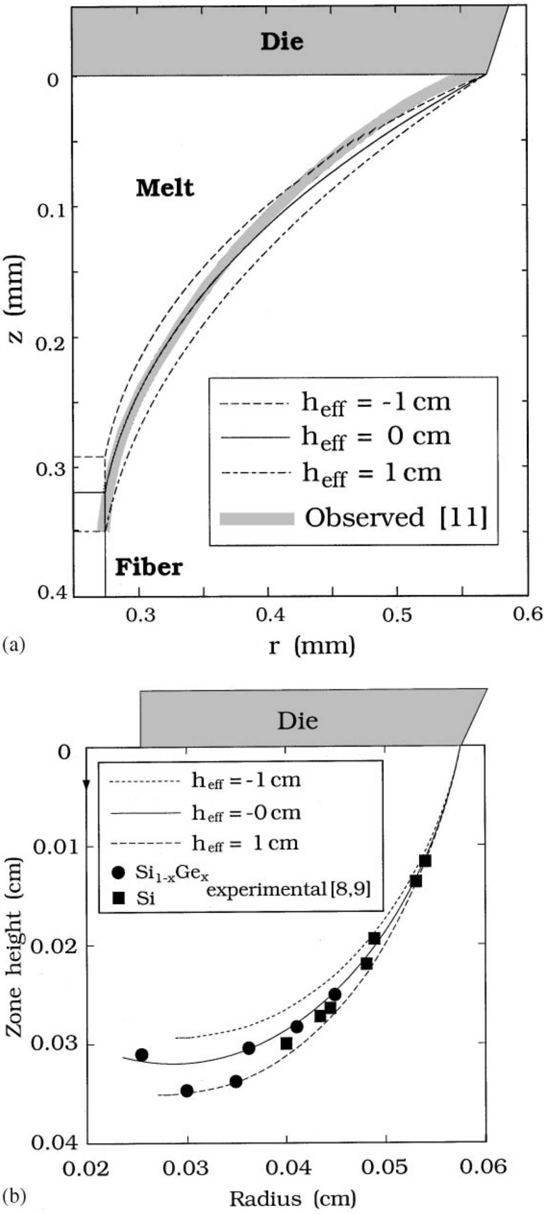

Fig. 3. (a) Meniscus shape for different h_{eff}'s; (b) relationship of zone height and grown radius for different h_{eff}'s.

shape is also depicted for comparison. For $h_{\mathrm{eff}} = 0$, the calculated shape is almost the same as that obtained from the low-Bo approximation (with an analytical solution), where the gravity effect is ignored [18]. This indicates that the effect of convection on the meniscus shape is trivial here. As compared with the observed shape, the agreement is reasonably good. In fact, the shape obtained by the CCD camera is not perfectly axisymmetric. More importantly, the wetting line at the melt/die junction is not clearly defined, which makes a better comparison difficult. The wetting angle with the die, i.e., θ_c (also see Fig. 2a), is slightly smaller than the Gibbs limit here; this limit is about 30° for the present case ($\phi_d = 120°$). Therefore, the dewetting is very likely.

The relationship of the zone height and the grown fiber size for different h_{eff}'s is summarized in Fig. 3b. This relationship is obtained by adjusting the die tip temperature $T_d|_0$. The experimental results are obtained from both the growth of Si [8] and $Ge_{0.5}Si_{0.95}$ [9]. As shown, the calculated results are in good agreement with the observed ones for the dimensional h_{eff} being between 0 and 1 cm. Therefore, it is believed that the gravity force still plays a role here. Furthermore, for the same zone height, there is another solution branch with a smaller radius ($R_c < 0.03$ cm). However, this branch is not stable according to Surek's stability criterion, and should be avoided during growth.

3.2. Effect of convection

Although the system is small, convection may still be important in such a small molten zone. To illustrate this, we have examined different convection modes and the calculated results are shown in Fig. 4. For this case, $T_d|_0 = 1676.4$ K, $D = 5.6 \times 10^{-5}$ cm^2/s, and $U_c = 3$ cm/h. The solute and flow fields are shown from Fig. 4a–Fig. 4c, while thermal fields from Fig. 4d to Fig. 4f. When the buoyancy and thermocapillary forces are turned off, the convection inside the melt is only due to the pulling of the fiber, as shown in Fig. 4a and Fig. 4d. As the buoyancy force is considered in Fig. 4b and Fig. 4e, two convection loops near the centerline and the free surface are induced. However, their intensities are very weak. The zero streamline is indicated by a dashed line with an asterisk. In fact, the excess Ge in front of the growth interface, being heavier at the bottom, stabilizes the system. As a result, the solute field is not affected much.

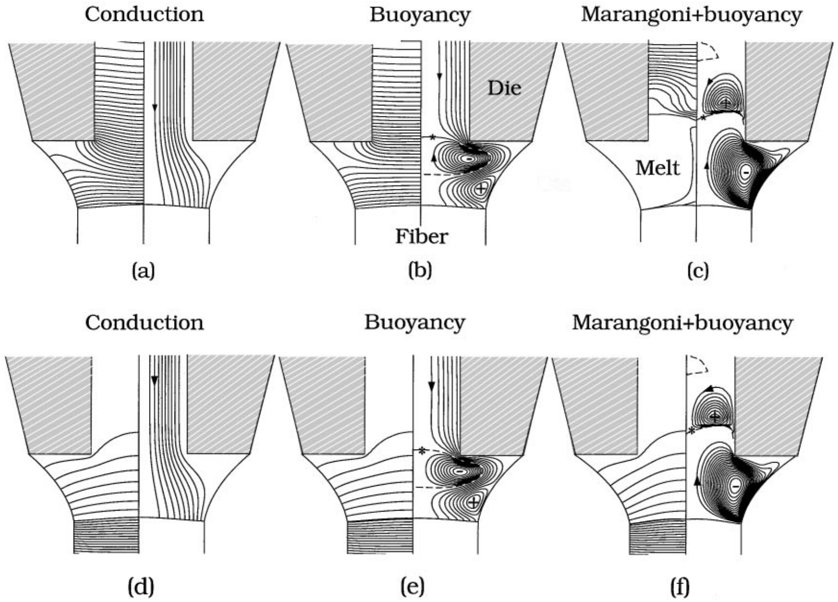

Fig. 4. Calculated fields for different convection modes: (a) and (d) for conduction only; (b) and (e) for buoyancy convection; (c) and (f) for both buoyancy and Marangoni convection. In the melt, $\Delta\psi = \psi_{\max}/10$ for positive ψ, $\Delta\psi = \psi_{\min}/20$ for negative ψ; $\Delta C = (C_{\max} - C_{\min})/50$, and $\Delta T = (T_{\max} - T_{\min})/10$. $\psi_{\min} = 0$, $\psi_{\max} = 4.203 \times 10^{-7}$ cm^3/s for (a), -3.965×10^{-7}, 6.475×10^{-7} cm^3/s for (b), and -0.001796, 5.146×10^{-6} cm^3/s for (c). $T_{\max} = 1683.4$, $T_{\min} = 1655.83$ K for (d), 1683.4, 1655.87 K for (e), 1683.4, 1655.32 K for (f). $C_{\min}/C_0 = 1$, $C_{\max}/C_0 = 2.5061$ for (a) 1, 2.5024 for (b) and 1, 2.5524 for (c) .$T_{\mathrm{d}}|_0 = 1676.4$ K.

However, as the thermocapillary force is considered, the effect becomes significant. As shown in Fig. 4c, the flow prevails in the melt zone. Because of the high temperature gradients near the growth interface, the induced melt speed is as high as 19.6 cm/s. In fact, such a high melt speed is not uncommon. In the calculations by Yeckel et al. [19] for floating-zone Si sheet growth, the same order of the melt speed was reported. As a result, the solute is well mixed in the molten zone. Outside the main flow loop, a small secondary cell is induced, and the solute fields are also affected there. However, further inside the hole, the solute mixing is poor, where the diffusion is dominant. The thermal field is also affected by the thermocapillary flow as well, as shown in Fig. 4f. Heat is delivered more effectively from the die to the fiber at the surface, which can be seen from the more distortion of the isotherms near the meniscus. As a result, the melt zone at the surface becomes longer and thus the grown fiber diameter is reduced.

It should be pointed out that as mentioned previously for Fig. 3b, the solution obtained in Fig. 4 is not unique. A set of solution with a much smaller fiber diameter is also obtained, and the multiplicity is mainly due to the nonlinear capillary statics [9]. According to the Surek's stability criterion, this solution is not stable.

3.3. *Effect of pulling rate*

Different pulling rates are considered and their effects on the radial solute distribution in the melt are illustrated in Fig. 5. The flow and solute fields are also shown in the same figure. As shown in the solute fields, with a higher pulling rate, the solute gradients in the hole are higher. Because of the larger solute gradients, as expected, the radial solute segregation increases with the increasing growth rate. At $U_{\mathrm{c}} = 6$ cm/h, the excess of Ge near the centerline also causes the interface depression there due to the lower liquidus temperature. In

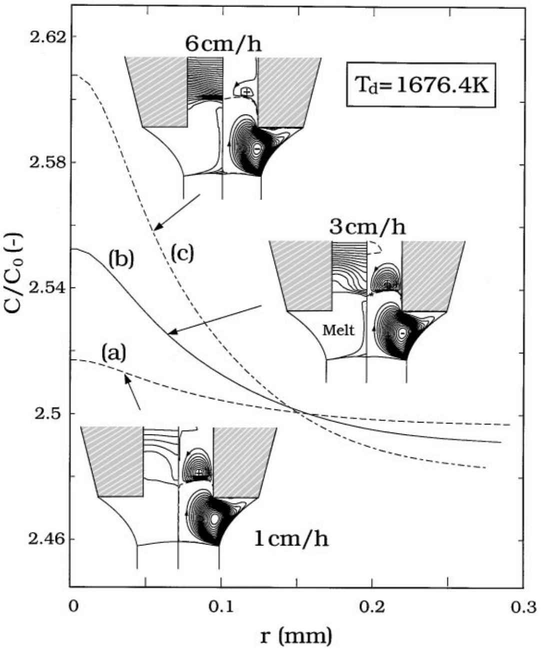

Fig. 5. Radial Ge distributions for different growth rates. For the field plots, $C_{\min}/C_0 = 1$, $C_{\max}/C_0 = 2.5171$, $\psi_{\min} = -0.001848$, $\psi_{\max} = 8.4171\times10^{-6}\ \mathrm{cm^3/s}$ for (a), $C_{\min}/C_0 = 1$, $C_{\max}/C_0 = 2.5524$, $\psi_{\min} = -0.001796$, $\psi_{\max} = 5.1464\times10^{-6}\ \mathrm{cm^3/s}$ for (b), and $C_{\min}/C_0 = 1$, $C_{\max}/C_0 = 2.6077$, $\psi_{\min} = -0.0017$, $\psi_{\max} = 5.440\times10^{-6}\ \mathrm{cm^3/s}$ for (c).

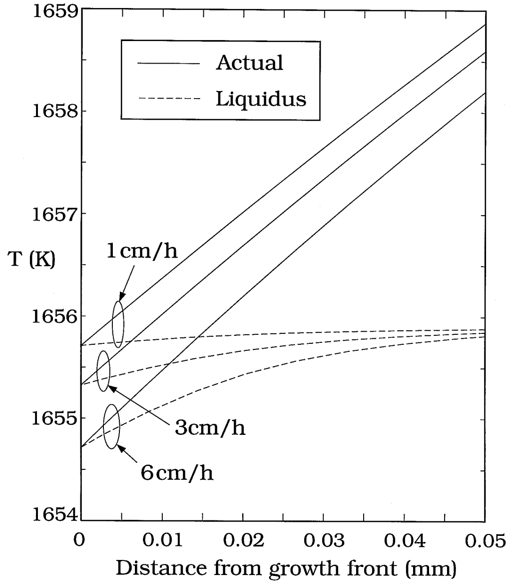

Fig. 6. Actual and liquidus temperature distributions in the melt at the centerline for different growth rates.

addition to the segregation, the increase of the pulling rate also reduces the grown fiber diameter, which can be seen from the field plots. Clearly, the more release of the heat of fusion results in a longer zone, and hence the smaller fiber diameter. Due to the increased necking of the meniscus with the increasing pulling rate, the Marangoni convection can penetrate more into the hole region, which can be seen by the location of the zero streamline and the diminishing of the secondary cell.

In practice, a major concern for the high growth rate in crystal growth is the onset of constitutional supercooling. To illustrate the possibility of the supercooling, the actual and liquidus temperature profiles at the centerline from the growth front for different growth rates are plotted in Fig. 6. As shown, although we do not observe any supercooling for these three growth rates, the possibility of the supercooling becomes higher with the increasing growth rate, which can be seen from the angle between two profiles at the growth front. Furthermore, the thermal gradients at the growth front are as high as 700 K/cm. Because of the lower crystal thermal conductivity, the thermal gradients in the crystal side are up to 2000 K/cm. Because of the high thermal gradients, a high growth rate is usually allowed for fiber growth.

3.4. *Effect of die tip temperature*

During crystal growth experiments, it was observed that the control of the fiber diameter through the heater power (die temperature) is very effective. From Fig. 3b, it is obvious that the shorter the zone (the less power), the larger the grown fiber diameter. Therefore, calculations for $T_{\mathrm{d}} = 1675.4$ and 1673.4 K are also conducted, and the calculated results as well as that for $T_{\mathrm{d}} = 1676.4$ K are summarized in Fig. 7 for comparison. From the field plots, the zone length decreases with the decreasing die temperature leading to a larger fiber diameter. As the zone length decreases, the Marangoni convection becomes less likely to penetrate into the zone center. Instead, a secondary cell is induced. Due to the secondary flow cell, the

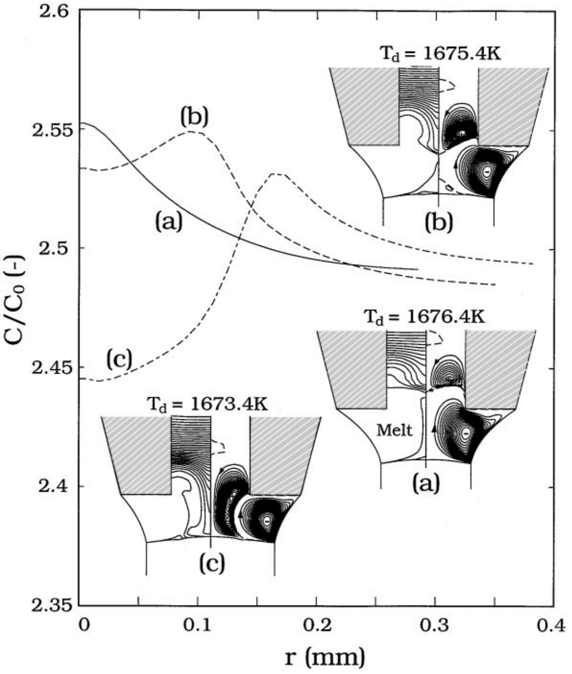

Fig. 7. Radial Ge distributions for different die temperatures. For the field plots, $C_{\min}/C_0 = 1$, $C_{\max}/C_0 = 2.5524$, $\psi_{\min} = -0.001796$, $\psi_{\max} = 5.1464 \times 10^{-6}$ cm^3/s for (a), $C_{\min}/C_0 = 1$, $C_{\max}/C_0 = 2.5490$, $\psi_{\min} = -0.002121$, $\psi_{\max} = 2.0884 \times 10^{-5}$ cm^3/s for (b), and $C_{\min}/C_0 = 1$, $C_{\max}/C_0 = 2.5324$, $\psi_{\min} = -0.002070$, $\psi_{\max} = 2.7146 \times 10^{-5}$ cm^3/s for (c).

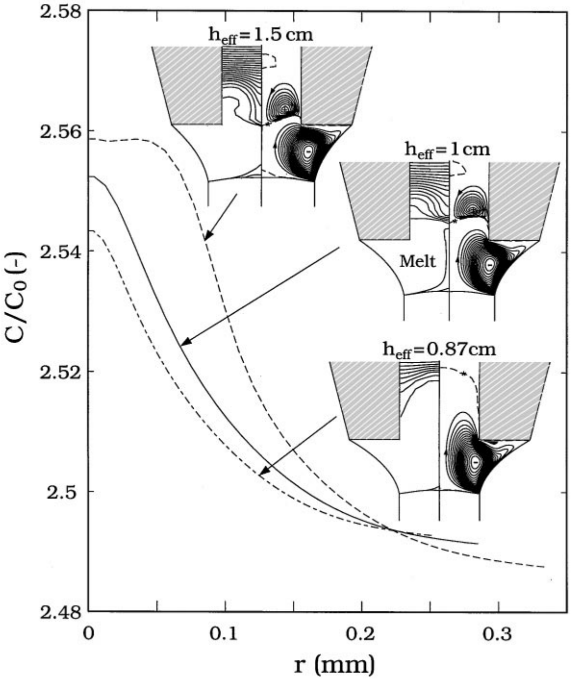

Fig. 8. Radial Ge distributions for different h_{eff}'s. For the field plots, $C_{\min}/C_0 = 1$, $C_{\max}/C_0 = 2.5586$, $\psi_{\min} = -0.00222$, $\psi_{\max} = 2.1067 \times 10^{-6}$ cm^3/s for $h_{\text{eff}} = 1.5$ cm, $C_{\min}/C_0 = 1$, $C_{\max}/C_0 = 2.5524$, $\psi_{\min} = -0.001796$, $\psi_{\max} = 5.1464 \times 10^{-6}$ cm^3/s for $h_{\text{eff}} = 1$ cm, and $C_{\min}/C_0 = 1$, $C_{\max}/C_0 = 2.5434$, $\psi_{\min} = -0.001463$, $\psi_{\max} = 5.2822 \times 10^{-6}$ cm^3/s for $h_{\text{eff}} = 0.87$ cm.

solute segregation behavior is greatly changed. As shown, the radial solute distribution is reversed when the die temperature is reduced to 1673.4 K. This inversion of the segregation and the depletion of Ge at the centerline were also observed in the growth experiments [12] when the fiber diameter was increased by reducing the die temperature.

We also have conducted calculations for smaller $|\partial\gamma/\partial T|$. Interestingly, the secondary cell is much harder to induce and, therefore, no inversion of the segregation is observed.

3.5. *Effect of melt height*

As mentioned previously, the grown fiber amount is usually about 1 or 2% of the initial charge to the crucible. As a result, the melt height during the growth does not change much. However, its value can affect the meniscus shape and the fiber size as shown in Fig. 3. Because of the change of the meniscus shape and the fiber diameter by the melt height, heat transfer can be changed as well. To further illustrate the effect of the effective melt height h_{eff} for the same die temperature and the growth rate ($T_{\text{d}} = 1676.4$ K and $U_{\text{c}} = 3$ cm/h), additional calculations are performed for $h_{\text{eff}} = 0.87$ and 1.5 cm, and their calculated results as well as that for $h_{\text{eff}} = 1$ cm are illustrated in Fig. 8. As shown from the field plots, when h_{eff} is reduced slightly to 0.87 cm from 1 cm, the grown fiber diameter is significantly reduced. Because of the too small fiber diameter, this case is believed to be unstable. According to the analysis by Tatarchenko [18], the maximum stability of the meniscus is expected at $R_{\text{c}} \approx 0.8R_{\text{d}}$, and also from Fig. 3b, the fiber radius is very sensitive to the melt height when

$R_c \approx 0.5R_d$. Furthermore, based on the Surek's stability criterion [14] for capillary shaping, this case is not stable due to $dh_c(1)/dR_c < 0$. On the other hand, the increase rate of R_c per unit change of h_{eff} to 1.5 cm is smaller than that to 0.87 cm. Clearly, keeping R_c away from the point of $dh_c(1)/dR_c = 0$ makes the grown fiber radius less sensitive to the melt height. Similar observation was found during crystal growth experiments. However, with the increasing fiber diameter, the radial solute segregation increases.

4. Conclusions

We have developed a numerical model to analyze the micro-pulling-down growth of Ge_xSi_{1-x} fibers. The steady-state heat and mass transfer, melt flow, interface shapes, as well as the grown fiber diameter, are computed simultaneously using a robust finite-volume/Newton's method. The present analysis provides a direct view of the melt flow and solute transport in such a small system as well as a detailed understanding of the process. The calculated results can also be used directly to the inverse edge-defined film-fed growth process.

The calculated fiber grown radius as a function of the zone length is in good agreement with measurements. A reasonable agreement for the meniscus shape is obtained as well. For the case with a zero effective melt height, the calculated meniscus shape is almost identical with the analytical solution using the low-Bo approximation, which indicates that the melt convection is not important at all on the meniscus shape. The melt flow in the hole is not affected much by the convection in the zone region. The calculated axial solute distribution in the zone region and the hole for the case without buoyancy and thermocapillary convections is in good agreement with that calculated using a plug flow approximation. In the zone region, the buoyancy convection is extremely weak due to the small physical dimension and the damping effect by the excess and heavier Ge segregated in the melt. However, thermocapillary convection is still strong in the melt zone leading to a solute mixing there. Unfortunately, such a mixing often causes a larger segregation. Furthermore, the segregation increases with the increasing growth rate. More interestingly, decreasing the die temperature or increasing fiber radius could result in an inversion of the radial solute segregation as well as the depletion of Ge at the fiber center due to the formation of the secondary cell induced by the thermocapillary flow. This inversion was also observed in experiments. Finally, we have also shown that the grown fiber radius is affected by the melt height. This indicates that different initial charges can grow the fibers with different diameters. If the grown radius is less than half of the die radius, the dynamic instability occurs. For the same growth parameters, the grown fiber radius increases with the increasing melt height.

Acknowledgements

The authors are grateful for the support of National Science Council of ROC under Grant No. NSC84-2112-M-007-050PH through National Tsing-Hua University. The computing facilities supported by the National Center for High Performance Computing are highly appreciated. C.W.L. also acknowledges the full financial support by the No. 161 committee of the Japanese Society for Promotion of Science to present some of this work in the International Symposium on Laser and Nonlinear Optical Materials 1997 held in Singapore.

References

[1] L. Hesselink, S. Redfield, Opt. Lett. 13 (1988) 877.

[2] S. Sudo, I. Yokohama, A. Cordova-Plaza, M.M. Fejer, R.L. Byer, Appl. Phys. Lett. 56 (1990) 1931.

[3] H. Yoshinaga, K. Kitayama, Appl. Phys. Lett. 56 (1990) 1728.

[4] R.S. Feigelson, Growth of Fiber Crystals, in: E. Kaldis (Ed.), Crystal Growth of Electronic Materials, North-Holland, Amsterdam, 1985, p. 127.

[5] D.H. Yoon, I. Yonenaga, T. Fukuda, N. Ohnishi, J. Crystal Growth 142 (1994) 339.

[6] Y.M. Yu, V.I. Chani, K. Shimamura, K. Inaba, T. Fukuda, J. Crystal Growth 77 (1997) 74.

[7] B.M. Epelbaum, K. Inaba, S. Uda, T. Fukuda, J. Crystal Growth 179 (1997) 559.

[8] K. Shimamura, S. Uda, T. Yamada, S. Sakaguchi, T. Fukuda, Jpn. J. Appl. Phys. 35 (1996) 703.

[9] N. Schafer, T. Yamada, K. Shimamura, H.J. Koh, T. Fukuda, J. Crystal Growth 166 (1996) 675.

[10] B.M. Epelbaum, K. Shimamura, S. Uda, J. Kon, T. Fukuda, Crystal Res. Technol. 31 (1996) 1077.

[11] H.J. Koh, N. Schafer, K. Shmamura, T. Fukuda, J. Crystal Growth 167 (1996) 38.

[12] S. Uda, J. Kon, K. Shimamura, T. Fukuda, J. Crystal Growth 167 (1996) 64.

[13] C.W. Lan, J. Crystal Growth 169 (1996) 269.

[14] T. Surek, B. Chalmers, J. Crystal Growth 29 (1975) 1.

[15] C.W. Lan, Int. J. Numer. Meth. Fluids 19 (1994) 19.

[16] M.C. Liang, C.W. Lan, J. Comp. Phys. 127 (1996) 330.

[17] H. Kodera, Jpn. J. Appl. Phys. 2 (1963) 212.

[18] V.A. Tatarchenko, E.A. Brener, J. Crystal Growth 50 (1980) 33.

[19] A. Yeckel, A.G. Salinger, J.J. Derby, J. Crystal Growth 152 (1995) 51.